

# Driven phase space holes and synchronized Bernstein, Greene, and Kruskal modes

L. Friedland<sup>a)</sup>

*Racah Institute of Physics, Hebrew University of Jerusalem, Jerusalem 91904, Israel*

F. Peinetti, W. Bertsche, J. Fajans, and J. Wurtele

*Department of Physics, University of California at Berkeley, Berkeley, California 94720*

(Received 25 March 2004; accepted 15 June 2004; published 16 August 2004)

The excitation of synchronized Bernstein, Greene, and Kruskal (BGK) modes in a pure electron plasma confined in Malmberg–Penning trap is studied. The modes are excited by controlling the frequency of an oscillating external potential. Initially, the drive resonates with, and phase-locks to, a group of axially bouncing electrons in the trap. These initially phase-locked electrons remain phase-locked (in “autoresonance”) during a subsequent downward chirp of the external potential’s oscillation frequency. Only a few new particles are added to the resonant group as the frequency, and, hence, the resonance, moves to lower velocities in phase space. Consequently, the downward chirp creates a charge density perturbation (a hole) in the electron phase space distribution. The hole oscillates in space, and its associated induced electric field constitutes a BGK mode synchronized with the drive. The size of the hole in phase space, and thus the amplitude of the mode, are largely controlled by only two external parameters: the driving frequency and amplitude. A simplified kinetic theory of this excitation process is developed. The dependence of the excited BGK mode amplitude on the driving frequency chirp rate and other plasma parameters is discussed and theoretical predictions are compared with recent experiments and computer simulations. © 2004 American Institute of Physics. [DOI: 10.1063/1.1781166]

## I. INTRODUCTION

The excitation and control of large amplitude waves is one of the most important goals of both basic and applied plasma research. Waves can emerge spontaneously from internal perturbations via instabilities, but such processes are largely controlled by the plasma state and trap geometry. Alternatively, with much greater controllability, waves can be excited by external driving sources. Experimentally, some types of waves are easier to excite than others. For example, plasma waves in finite geometry [Trivelpiece–Gould (TG) modes<sup>1</sup>] can be generated easily by external drives, but these waves are often strongly Landau damped. In contrast, Bernstein, Greene, and Kruskal (BGK) (Ref. 2) predicted the existence of a large class of *undamped* kinetic waves (BGK modes) in collisionless plasmas, but after nearly five decades of studies (see, for example, Ref. 3 and references therein), the experimental generation of large amplitude BGK modes has proven difficult. The reason is simple: BGK showed that for a given proscribed plasma particle velocity distribution, there exists a self-consistent dissipationless traveling wave form, or, conversely, a proscribed BGK wave form will only be dissipationless for an appropriate velocity distribution. In experiments, however, one depends on initial-boundary conditions for *both* the particle distributions and the wave forms, and these twofold initial conditions do not necessarily correspond to a BGK mode. As a consequence, one can easily create *transient*, large amplitude kinetic structures in plasmas, but these waves are frequently unstable and shortlived,

and do not necessarily relax to a BGK mode. For example, large amplitude waves created by Wharton, Malmberg, and O’Neil<sup>4</sup> were unstable due to a sideband instability. More recent work has not been any more successful.<sup>5,6</sup> Nevertheless, long-lasting structures can be created by continuous drives, and driven double layers, which are related to BGK modes, have been observed in the earth’s auroral zone.<sup>7</sup> Also, Danielson<sup>8</sup> recently reported that plasma waves eventually decay into low amplitude, but long-lasting BGK modes. Finally, spontaneously generated pairs of BGK modes, upshifting and downshifting in frequency near a kinetic instability threshold were predicted and investigated theoretically by Berk *et al.*<sup>9–12</sup> In the present work we propose a different mechanism of efficient excitation and *control* of BGK modes. We start in a *stable* equilibrium, but apply an external, oscillating, chirped frequency drive. The idea is to adiabatically relocate a low density region of resonantly trapped electrons in phase space (the resonant bucket) from the tail of the distribution to the bulk. This slow relocation process creates a localized, growing depth depression in the original phase space distribution, while the charge density perturbation associated with this depression yields a BGK mode synchronized with the drive.

Our theory is motivated by recent experiments,<sup>13</sup> suggesting that large amplitude BGK modes can be *generated* and *controlled*, for certain experimental parameters, in trapped, pure electron plasmas. The modes are excited by an external, chirped frequency oscillating voltage which passes through the electron bounce frequency resonances. Figure 1 shows the experimental setup in Ref. 13, while Figs. 2 and 3 present the measured responses from the plasma in two dif-

<sup>a)</sup>Electronic mail: lazar@vms.huji.ac.il

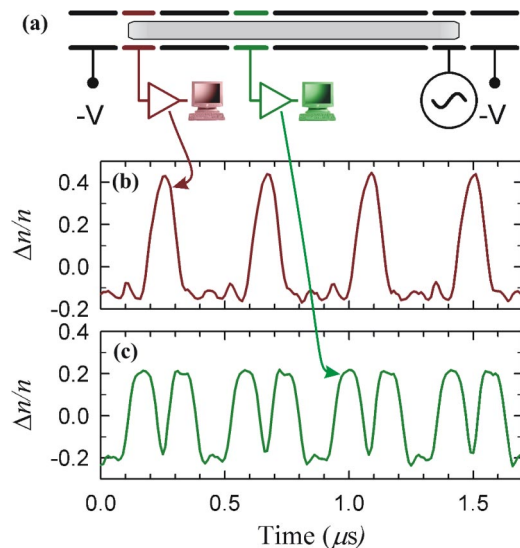


FIG. 1. (a) Penning-Malmberg Trap geometry in Ref. 13. The pure-electron plasma column is confined axially by the large negative end potentials, and radially by a 1500 G magnetic field. Typical plasma densities are  $\sim 10^7 \text{ cm}^{-3}$ , lengths  $\sim 27 \text{ cm}$ , and radii  $\sim 1 \text{ cm}$ , and the plasma is confined in cylinders with radius 1.905 cm. (b) Density fluctuations due to the BGK mode at the column end, and (c) near the column center. The positive fluctuations corresponds to electron holes. Because the BGK mode must pass through the center twice (approaching and leaving) each time the pulse reaches the end, there are twice as many pulses in (c) as in (b). As expected for an open-ended reflection, the mode is larger at the end (b) than near the center (c).

ferent experimental settings with the same (50 mV) amplitude drives, but constant and down-chirped frequencies, respectively. The results in Fig. 2, which display the response to a slowly scanning, constant frequency drive, were interpreted as driven TG modes with multiple peaks associated with different mode numbers. Note that in these experiments,  $\omega_p \ll \omega_c$ ,  $\omega_p$ , and  $\omega_c$  being the plasma and cyclotron frequencies. Thus, we are well below the Brillouin density limit<sup>14</sup> and can neglect the plasma rotation on the dispersion characteristics of the excited plasma waves. On the other hand, the small aspect ratio  $R/L \ll 1$  of the plasma ( $R$  and  $L$  being the plasma radius and length) allows one to neglect geometric plasma end effects on the dispersion. Under these conditions,

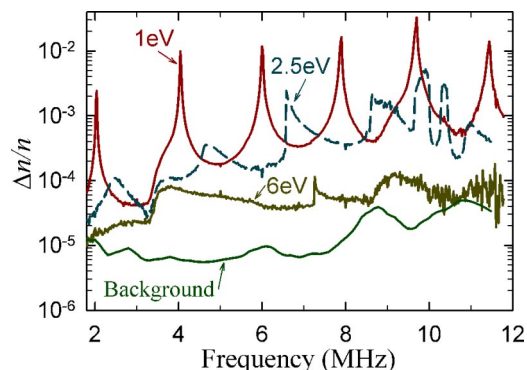


FIG. 2. Observed (see Ref. 13) response from a pure 50 mV drive, for three different plasma temperatures. Also shown is the background noise from external sources. The multiple picks in the spectrum correspond to different excited TG mode numbers.

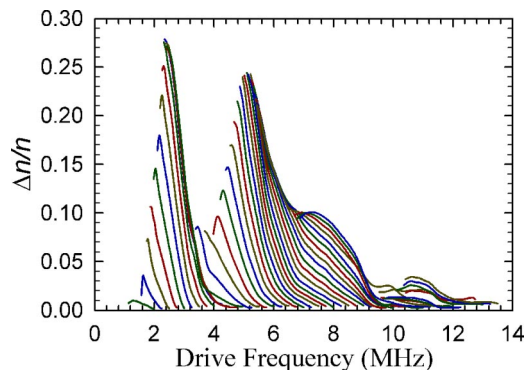


FIG. 3. Response to 50 mV, 1 GHz/s swept frequency drives (see Ref. 13). Each curve plots the envelope of the response as a function of time, and hence, frequency, as the sweep progresses downward from each plot's individual start frequency  $f_s$ . Along each curve, the response is phase locked to the drive. As the drive is swept past the peaks at 2.4 MHz and 5 MHz, phase locking is lost and the mode amplitude collapses.

we expect the TG mode dispersion relation in the non-neutral plasma to be similar to that in an infinitely long neutral plasma, having similar parameters, i.e.,  $\omega^2 = \omega_m^2 + 3v_{th}^2 k^2$ , where  $\omega_m = [a^2 k^2 \omega_p^2 / (1 + a^2 k^2)]^{1/2}$  are the cold TG mode frequencies,  $a$  is the radial geometric constant, the wave number  $k = (m+1)\pi/L$  ( $m=0, 1, 2, \dots$ ) is dictated by the plasma length, and  $v_{th}$  is the electron thermal velocity. Note also that in our small aspect ratio plasma,  $ak \ll 1$ , i.e.,  $\omega \ll \omega_p$ . The largest relative density excitations,  $\Delta n/n$  of a few percent in Fig. 2, occur at electron temperatures of  $T_e = 1 \text{ eV}$ ; as the temperature increases, the response decreases sharply and practically disappears at  $T_e = 6 \text{ eV}$ . After the drive ceased, these TG modes had typical  $Q$  factors of less than 600, even at  $T_e = 1 \text{ eV}$ . In contrast, in experiments with the down-chirped frequency drive (Fig. 3), at  $T_e = 6 \text{ eV}$ , the relative driven density variation peaked at  $\Delta n/n = 27\%$  (and even at 40% with slightly different conditions), while the observed  $Q$  was up to 100 000. These high  $Q$  excitations were robustly phase locked to the drive and, thus, could be easily controlled by changing the form of the frequency chirp. For example, the emerging large wave forms could be returned adiabatically to nearly their initial, small amplitude states by simply reversing the direction of variation of the driving frequency. We interpreted these driven, phase-locked excitations as BGK modes, with the excitation mechanism related to resonant dynamics of a part of the electron phase-space distribution in the trap in the presence of the chirped frequency drive. A number of additional experimental results were discussed in Ref. 13, all supporting the proposed excitation mechanism.

Our main goal here is to explain the results of these experiments, particularly the difference between Figs. 2 and 3 and the effect of the plasma temperature on the basis of a simple model. In Sec. II we study the resonant dynamics of a one-dimensional (1D), initially Maxwellian electron gas trapped in a square well potential and driven by a chirped frequency external potential. We shall neglect the self-field in the system at this stage of the analysis. Initially, the drive resonates with a group of particles in the tail of the distribution. Subsequently, the resonant region moves into the bulk

of the distribution as the driving frequency decreases. We show in Sec. II that for a constant drive amplitude and linear frequency chirp, all initially resonant (phase-trapped) particles remain trapped at later times, and no new particles are added to the resonant group (bucket) as it moves in phase space. Since the *initially* trapped electrons are from the tail of the velocity distribution, their density is relatively small. Therefore, as the resonant bucket reaches the bulk of the distribution, it creates a localized depression (hole) in the electron density in phase space (see Fig. 5 below). At the same time, the electron velocity distribution develops a local depression with a width corresponding to the bucket in the phase space (see Fig. 6) and a minimum at the exact resonance. The growth of this hole yields the growing driven BGK mode.

In Sec. III, we add self-consistency to the resonant bucket dynamics. We employ a full Vlasov-Poisson system, and work in the action-angle variables associated with our model of bouncing electrons. The theory assumes that the driving and self-fields are small, but uses a *non-perturbative*, space-averaged distribution with a parabolic depression at the exact resonance. Then we derive an expression for the adiabatically varying amplitude of the BGK mode excited by chirped frequency drive, and compare our predictions with experiments. Section IV describes self-consistent numerical simulations of chirped-bucket BGK modes. The simulations allow us to check the stability of our model, to test predictions of the small amplitude theory, and to better visualize large amplitude excitations, yielding a more accurate comparison with experiments. Finally, Sec. V presents our conclusions.

## II. CHIRPED, RESONANT BUCKET DYNAMICS

In this section we study bounce-resonant dynamics of a pure electron plasma in the trap, shown schematically in Fig. 1. We assume an axisymmetric, small aspect ratio configuration,  $R/L \ll 1$  ( $R$  and  $L$  are the radius and the length of the plasma column), and use the driving potential of form  $\varphi_d = V(z, r) \cos[\psi_d(t)]$ , where the driving frequency  $\omega_d(t) = d\psi_d/dt = \omega_0 - \alpha t$  is linearly down chirped in time, with the chirp rate  $\alpha$ . We assume that the electrons are strongly confined to the magnetic field lines, and neglect the effect of the radial structure of the longitudinal electric field on the electron dynamics, i.e., we assume that  $\kappa r \ll 1$  for the electrons in the plasma,  $\kappa$  being the characteristic inverse radial scale of variation of the electric field. This makes electron dynamics in our model one-dimensional (1D) and driven by a one-dimensional potential

$$\varphi_d = \varphi_0(z) \cos[\psi_d(t)], \quad (1)$$

where  $\varphi_0(z) \approx V(0, z)$ . We further neglect the end effects in the trap and model the external trapping potential as a square well of length  $L$ . Initially, we assume a uniform density  $n_0$  of the electrons and normalized Maxwellian distribution of longitudinal electron velocities  $f_0(|v|) = 2(\sqrt{2\pi}v_{th})^{-1} \times \exp[-\frac{1}{2}(|v|/v_{th})^2]$ ,  $v_{th}$  being the thermal velocity. Our goal is to describe the evolution of the electron distribution in phase space due to the chirped frequency drive, neglecting,

at this stage, the self-electric field, which will be considered in Sec. III. We assume that the driving field amplitude is small, i.e., for  $[(e/m)\varphi_0]^{1/2} \ll v_{th}$ .

The electron dynamics in our 1D problem are governed by the Hamiltonian

$$H(p, z, t) = \frac{p^2}{2m} - e\varphi_0(z) \cos[\psi_d(t)], 0 \leq z \leq L. \quad (2)$$

The bounce frequency of the unperturbed electrons in the well is  $\Omega = \pi|v|/L$ . We are interested in the transient, nonlinear resonance phenomenon taking place as the driving frequency passes through bounce-resonances  $n\Omega = \omega_d(t)$ ,  $n = 1, 2, \dots$ . Therefore, it is convenient to transform from the  $(p, z)$  variables in Eq. (2) to the canonical action-angle variables  $(I, \theta)$  of the unperturbed problem. The transformation is simple:  $p = \pi I/L$ ,  $z = L/\pi \Theta$  for  $0 \leq \Theta < \pi$ , and  $z = L/\pi(2\pi - \Theta)$  for  $\pi \leq \Theta < 2\pi$ , where  $\Theta = \text{mod}(\theta, 2\pi)$ . The transformed Hamiltonian (2) becomes

$$H = \frac{1}{2} \mu I^2 - \cos[\psi_d(t)] \sum_{n=1}^{\infty} 2\varepsilon_n \cos(n\theta), \quad (3)$$

where we have expanded  $e\varphi_0(z)$  ( $\phi$  is an even function in  $\Theta$  around  $\Theta = \pi$ ) in a Fourier series. Our assumption of the square well trapping potential greatly simplifies the perturbing part of the Hamiltonian, which in this case depends on the angle variable  $\theta$  only. A different trapping equilibrium would introduce an additional dependence on action variable  $I$  in the potential in Eq. (3), complicating the solution discussed below.

Now, we focus on the resonance in the problem, i.e., consider particles, such that  $n\Omega \approx \omega_d(t)$ , and treat each resonant group via the *single resonance* approximation.<sup>15</sup> In other words, we describe the interaction of the electrons with the  $n^{\text{th}}$  component of the drive by Hamiltonian, obtained by retaining only one resonant term in Eq. (3),

$$H_n = \frac{1}{2} \mu I^2 - \varepsilon_n \cos[n\theta - \psi_d(t)]. \quad (4)$$

The frequency chirp rate  $\alpha$  is assumed to be small enough that, near a given time  $\tau$ , the dynamics can be viewed as a weak perturbation of a similar system in which the drive frequency assumes the constant value  $\omega_d(\tau)$ . Then one expects the single resonance approximation to be valid, as long as the adjacent resonances do not overlap.<sup>15</sup> We consider the dynamics under this approximation next, and will return to the problem of resonance overlap at the end of this section.

The Hamiltonian (4) yields the following evolution equations:

$$dI/dt = -n\varepsilon_n \sin \Phi; \quad d\Phi/dt = nI - \omega_d(t), \quad (5)$$

where, here and in the following, dimensionless dependent and independent variables and parameters are introduced (with the same notations, for simplicity), i.e.,  $t \rightarrow \Omega_{th} t$ ,  $I \rightarrow I/I_{th}$ ,  $\omega_d \rightarrow \omega_d/\Omega_{th}$ ,  $\varepsilon_n \rightarrow \varepsilon_n/(mv_{th}^2)$ , and  $\alpha \rightarrow \alpha/\Omega_{th}^2$ , where  $\Omega_{th} = \pi v_{th}/L$  and  $I_{th} = mLv_{th}/\pi$ . Note that parameter  $\mu$  scales out after these transformations. Next, we differentiate the second equation in (5) and use the first equation in the result, yielding

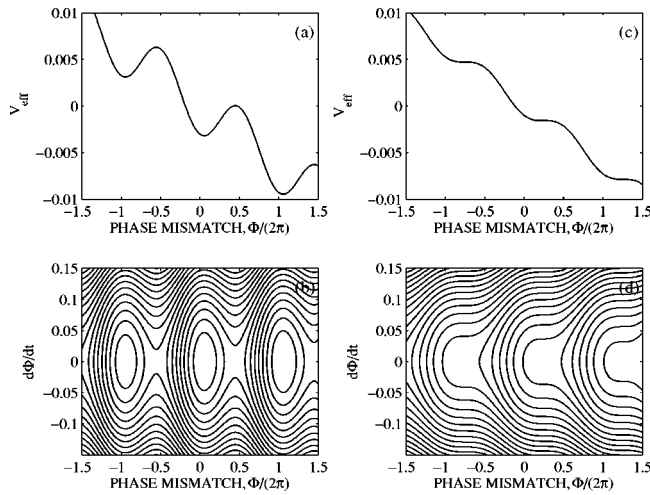


FIG. 4. The effective potential  $V_{\text{eff}}(\Phi)$  and the corresponding trajectories in  $(d\Phi/dt, \Phi)$ -space. (a,b):  $V_n=0.003$ ,  $\alpha=0.001$ . Potential wells and trapped trajectories in phase space exist in this case; (c,d): At critical conditions,  $V_n=0.001$ ,  $\alpha=0.001$ , the potential wells and trapped trajectories disappear.

$$d^2\Phi/dt^2 + V_n \sin \Phi - \alpha = 0, \quad (6)$$

where  $V_n = n^2 \varepsilon_n$ . This is an *autonomous* dynamical problem, describing the motion of a quasiparticle in an effective, time independent, tilted cosine potential

$$V_{\text{eff}} = -V_n \cos \Phi - \alpha \Phi. \quad (7)$$

Therefore, the dynamics of  $\Phi$  is integrable. We show the effective potential and the corresponding phase space  $(d\Phi/dt, \Phi)$  trajectories in Figs. 4(a)–4(d) for  $\alpha=0.001$  and two values  $V_n=0.003$  and  $0.001$ . If  $\alpha < V_n$  [Figs. 4(a) and 4(b)], the effective potential has potential wells with minima at  $\Phi_m$  given by  $\sin \Phi_m = \alpha/V_n$ . The depth of the wells is  $\Delta V = 2V_n \cos \Phi_m + 2\alpha\Phi_m - \alpha\pi$ . The potential wells divide the phase space into trapped and untrapped regions. The half width of the trapped regions in  $d\Phi/dt$  is  $\sqrt{2\Delta V}$ . Since  $d\Phi/dt = nI - \omega_d(t)$ , the half  $I$ -width of the trapped region (bucket) in  $(I, \Theta)$  space is  $\Delta I = \sqrt{2\Delta V}/n$ . When the driving frequency decreases, the resonant bucket *drifts* in this space at rate  $\alpha$  to smaller  $I$ , preserving its form at the same time. Finally, because of the time independence of  $V_{\text{eff}}$ , in case  $\alpha < V_n$ , all particles trapped initially in the wells will remain trapped, and no new particles will be added to the resonant group, despite the time variation of the driving frequency. If, in contrast,  $\alpha > V_n$  [in Figs. 4(c) and 4(d) the critical case  $\alpha = V_n$  is shown], the potential wells disappear and there are no trapped particles at any stage of evolution. We shall see below that the drift of the bucket to smaller  $I$  yields excitation of waves synchronized with the drive. One does not expect such waves when  $\alpha > V_n$ . We observed a similar threshold  $\varphi_0 > \varphi_{0th} \sim \alpha$  on the driving amplitude for efficient wave excitation in our experiments (see Fig. 7 in Ref. 13), and interpreted this threshold as one of the signatures of the trapping-in-resonant nature of the observed phenomenon.

Next, we calculate the effect of the chirped frequency driving on the normalized (to one) distribution  $f(I, \Theta, t)$  of electrons in phase space, still neglecting the self-field. The distribution is described by the Vlasov equation (we neglect

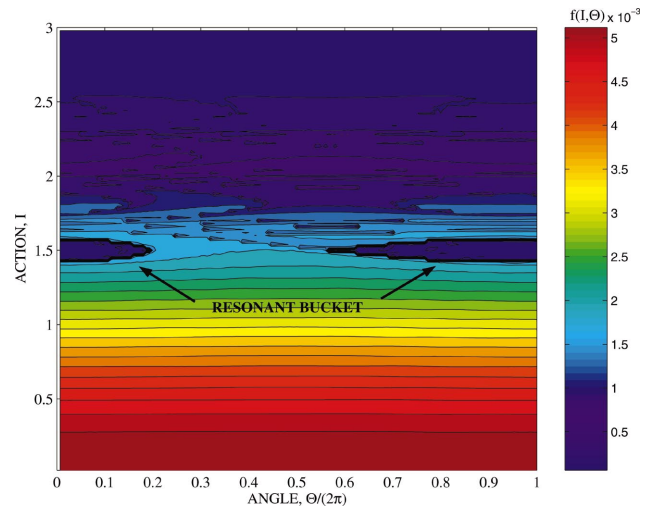


FIG. 5. (Color) The color map of the electron distribution  $f(I, \Theta)$  in phase space at final time  $t_f$ . The dark blue color of the resonant bucket at  $I_r=1.5$  indicates the origin of the trapped electrons, i.e., the tail of the distribution in the vicinity of the initial resonant action  $I_0=2.5$ .

collisions throughout our theory) and, therefore, is conserved along the trajectories in phase space. Consequently, one can find  $f$  at a given  $I, \Theta$ , and time  $t$ , by integrating equations of motion (5) backward in time, reaching  $t=0$ , and assigning the known initial distribution to this trajectory. This yields  $f(I, \Theta, t) = 2(2\pi)^{-3/2} \exp(-I_0^2/2)$ , where  $I_0$  is the value of the action at  $t=0$  on the trajectory starting with  $I, \Theta$  at time  $t$ . The results of the calculations based on these ideas are presented in Fig. 5. We focused on the fundamental ( $n=1$ ) resonance and integrated Eq. (5) from  $t=t_f$  to  $t=0$  successively, starting at  $150 \times 150$  uniformly distributed points in the region  $(I \in [0, 3], \Theta \in [0, 2\pi])$  in phase space yielding  $f(I, \Theta, t_f)$  on the uniform mesh, as described above. We used parameters  $\alpha=0.001$ ,  $V_1=0.003$  in the calculations and varied the driving frequency  $\omega_d$  between 1.5 (at  $t_f=1000$ ) and 2.5 (at  $t_0=0$ ). Figure 5 shows the resulting color map of  $f(I, \Theta, t=t_f)$ . One can see the resonant bucket centered at the final position of the resonance,  $\Omega_r = I_r = \omega_d(t_f) = 1.5$ . The dark blue color of the bucket indicates its origin, i.e., all the electrons in the bucket start in the tail of the initial distribution near  $I_0 = \omega_d(t_0) = 2.5$ . Prior to reaching the final position in Fig. 5, the bucket was oscillating in  $\Theta$  with the drive frequency and drifted in  $I$  at rate  $\alpha$ , as described above. All initially trapped electrons moved with the bucket and no new electrons were added to the resonant group as it drifted towards the bulk of the distribution. Since the electrons in the bucket were captured in the tail of the Maxwellian distribution, their density remained relatively low at the position of the bucket at later times, creating a growing depth local depression (hole) in the electron distribution in phase space. The original particles at the final position of the bucket were spread around and no significant change in the distribution outside the bucket is seen in Fig. 5. The increasing hole in the distribution is equivalent to an effective, growing, localized positive charge in the plasma, and the self-electric field associated with this charge constitutes a growing amplitude BGK mode (see Sec. III).

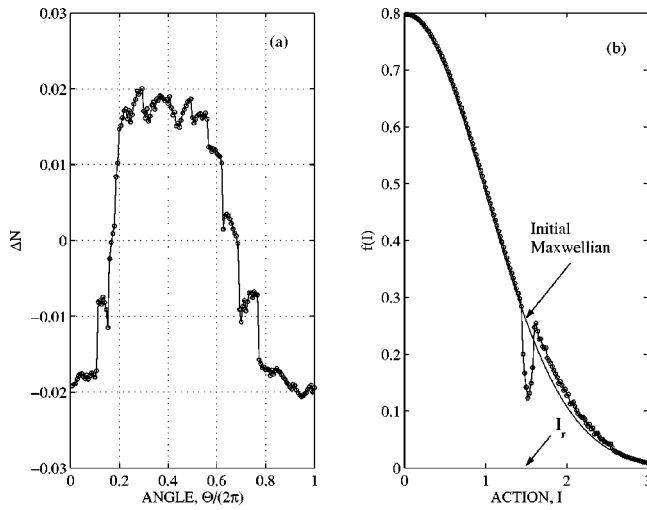


FIG. 6. The angle/space averaged distributions. (a) The normalized electron density perturbation  $\Delta N$  (circles) vs angle. (b) The space averaged electron distribution function  $f$  vs  $I$  (circles) at  $t=t_f$ . The initial Maxwellian distribution in the simulations is shown for comparison. The characteristic local depression in the driven distribution is seen with the minimum located at the exact resonance  $I=I_r$ .

For better illustration of this effect, we average  $f(I, \Theta, t=t_f)$  over  $I$ , yielding the normalized density  $N(\Theta)$  in  $\Theta$  space and show the density perturbation  $\Delta N(\Theta) = N(\Theta) - 1$  in Fig. 6(a). The plasma density perturbation as a function of position in the trap can be also obtained at this stage by folding  $\Delta N(\Theta)$  in  $\Theta$  around  $\Theta = \pi$  and adding the two parts of  $\Delta N$ . The electric field induced by this electron density perturbation is the excited BGK mode in the system (see Sec. III). Finally, we average  $f(I, \Theta, t=t_f)$  over  $\Theta$ , yielding the space-averaged normalized velocity distribution  $\bar{f}(I, t)$  of the electrons at  $t=t_f$  (recall that in dimensionless variables,  $v=I$ ), and show these results by dots in Fig. 6(b). The full line in the figure represents the original Maxwellian. Note the characteristic local depression in the distribution with the minimum located at the exact resonance  $I_r = \omega_d(t_f)$  at final time. The width of the resonant region is the same as the width  $2\Delta I$  of the resonant bucket discussed above. We have found in all our simulations that space-averaged distributions in the plasma driven by down-chirped frequency drives were always characterized, similar to Fig. 6(b), by a local minima in the resonant region. Based on these results, the theory of chirped-bucket BGK modes in Sec. III will use a heuristic, locally parabolic depression of the space-averaged distribution function in the resonant region, i.e.,

$$\bar{f}(I, t) \approx f_0(I_r) - h + \beta[I - I_r(t)]^2, \quad |I - I_r| < \Delta I, \quad (8)$$

where  $f_0(I_r)$  is the initial distribution at  $I_r(t)$ ,  $h(t)$  is the depth of the depression, and  $\beta = h(t)/\Delta I^2$ , in order to fit the width of the bucket to this model. One can estimate  $h(t)$  in Fig. 6 as the difference between the density of the electrons outside and inside the bucket at its center in  $I$  space, i.e.,  $h(t) \approx (1 - k)f_0(I_r) + kf_0(I_0)$ , where  $k$  is the fraction of  $2\pi$  occupied by the bucket at the exact resonance. Note that this depth is not a perturbation and, despite the assumed smallness of the driving amplitude,  $h$  may be of  $O(1)$  as the bucket enters the

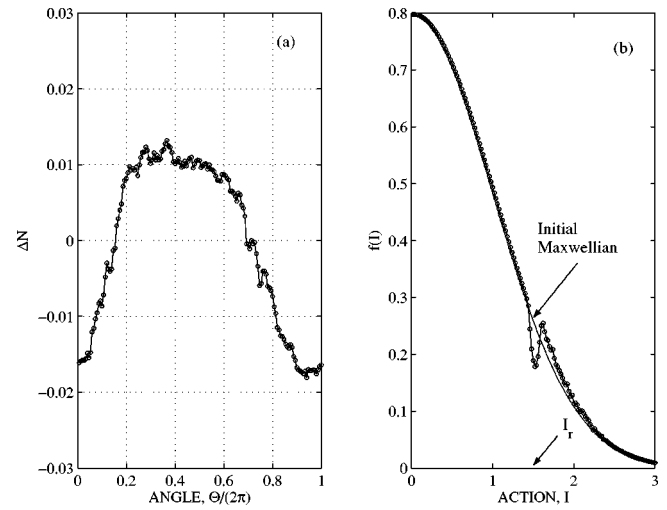


FIG. 7. The angle/space averaged distributions for linearly increasing driving amplitude  $\varepsilon_1 = \varepsilon_f t/t_f$  and all other parameters and initial conditions as those in Fig. 6. (a) The normalized electron density perturbation  $\Delta N$  (circles) vs angle. (b) The space averaged electron distribution function  $f$  vs  $I$  (circles) at  $t=t_f$ . The induced density perturbation and the depth of the resonant depression in the distribution function are smaller than those in Fig. 6 due to additional particles trapped in the drifting resonant bucket.

bulk of the distribution. The emergence of such *nonperturbative*, space-averaged distributions is the characteristic feature of trapped electron clouds driven by chirped frequency drives. Prior to using these distributions in the self-consistent theory, we consider two additional dynamical effects expected in resonantly driven plasmas even without inclusion of the self-field.

The first effect is that of a time varying amplitude of the driving field. One may increase the driving amplitude of mode  $n$  by external means. Alternatively, such an increase may be viewed as a *heuristic* addition of a phase locked, growing amplitude self-field of the same mode number. The evolution equations (5) in this case remain the same, but  $\varepsilon_1$  becomes a slow function of time. Assuming adiabaticity of  $\varepsilon_1$ , one preserves all initially trapped electrons in the bucket of growing size, but also adds new particles from the pool of untrapped electrons, as the bucket drifts in phase space. This phenomenon is illustrated in Figs. 7(a) and 7(b), showing the space-averaged distribution function for the same parameters and initial conditions as in Figs. 5 and 6, but with  $\varepsilon_1 = \varepsilon_f t/t_f$ , where  $\varepsilon_f = 0.003$ . We start with zero amplitude at  $t=0$  and the amplitude reaches that in Figs. 5 and 6 at  $t=t_f$ . We see in Fig. 7(b) that the width of the parabolic depression in the distribution, induced by a chirped frequency drive, is roughly the same as in Fig. 6(b), but the depth  $h$  of the minimum is smaller, since additional particles are now trapped in the bucket at its final position. As a consequence, the induced density perturbation [Fig. 7(a)] is also smaller than that for constant amplitude drive [Fig. 6(a)]. Nevertheless, the simulation shows that one can again approximate the space-averaged distribution in the resonant region by a parabolic profile (8) with a properly chosen  $h(t)$ .

The second important effect is the overlap of resonances. Until now, we have treated modes with different mode numbers  $n$  via the single resonance approximation. This approxi-

mation is applicable until the sum of the half widths of the adjacent (slowly drifting) resonances equals the distance between the centers of the resonances.<sup>15</sup> Quantitatively, the adiabatic nonoverlapping criterion for adjacent  $n, n+1$  resonances in our case is

$$\Delta I < I_r^n - I_r^{n+1} = \omega_d(t)/[n(n+1)]. \quad (9)$$

This condition is more restrictive for larger  $n$  and may be violated as the driving frequency decreases in time. Resonance overlap leads to chaotic mixing between the two adjacent resonant regions, invalidating the single resonance approximation. We expect such a mixing to result in a growing incoherence in the driven response and in the destruction of some modal components of the BGK wave in the self-consistent theory. In the limit  $\alpha \ll V_n$ ,  $\Delta I = 2\sqrt{V_n}/n$  and condition (9) limits the amplitudes of the neighboring coherent modes by inequality

$$(n+1)\sqrt{V_n} + n\sqrt{V_n} < \omega_d(t).$$

Let us now illustrate the effect of multiple resonances and resonance overlap phenomenon in chirped bucket dynamics via simulations. Again, we calculate the electron distribution in phase space by following the trajectories of a large number of particles with different initial conditions. Now, in contrast to Fig. 5, we include two additional resonances ( $n=2,3$ ) in the Hamiltonian, i.e., consider dynamics governed by

$$H_{1-2-3}(I, \theta) = \frac{1}{2}\mu I^2 - \sum_{n=1,2,3} \varepsilon_n \cos \Phi_n, \quad (10)$$

where the phase mismatches are  $\Phi_n = n\theta - \psi_d(t)$ . We use  $\varepsilon_{1,2,3} = 0.003$ ,  $\alpha = 0.001$ , and vary the driving frequency as before between  $\omega_f = 1.5$  and  $\omega_0 = 2.5$ . In this case, at  $t = t_f$ , the distance between the  $n=2$  and  $n=3$  resonances ( $I_r^{(2)} - I_r^{(3)} = 0.25$ ) is larger than the sum of the half-widths (0.123) of the resonances and one expects the single resonance approximation to work. A color map of the phase-space distribution function at final time in this example is shown in Fig. 8. We observe three resonant buckets at the corresponding resonant positions  $I_r^{(n)} = \omega_f/n = 1.50, 0.75, 0.50$ . The colors of the buckets indicate the origin of the resonant electrons: all came from the vicinity of initial resonant actions, at  $I = 2.50, 1.25, 0.83$ . There is a significant difference between the densities of the trapped electrons and those of the surrounding untrapped particles. This difference constitutes the existence of holes of different depths in the electron distribution in phase space. The corresponding normalized density perturbations  $\Delta N(\theta)$  in  $\Theta$  space and the space-averaged distribution function  $\bar{f}(I)$  are shown at  $t = t_f$  in Figs. 9(a) and 9(b), respectively.

The density perturbation in Fig. 9(a) is larger than in the single mode drive case [Fig. 6(a)]. Furthermore, it has a more complex structure, since it includes a larger number of spatial modes (see Fig. 12 below). One observes three separate depressions in the  $\bar{f}(I)$  distribution in Fig. 9(b), each having characteristic parabolic shape with a minima at  $I_r^{(1,2,3)}$ . These resonant regions have different depths, each depending on the initial and final positions of the corre-

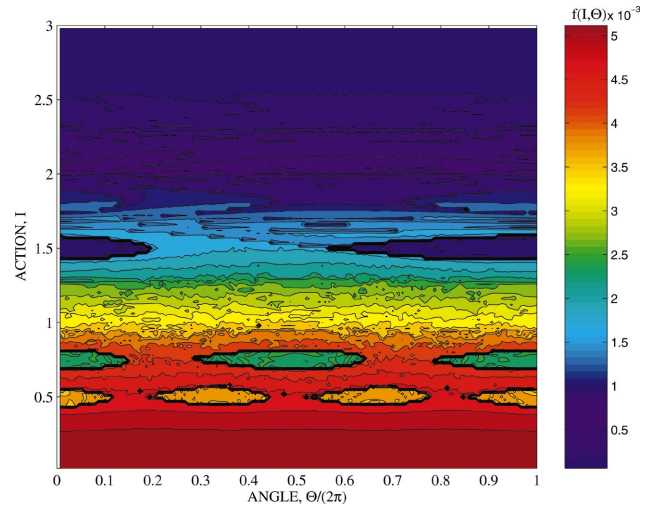


FIG. 8. (Color). The color map of the electron distribution  $f(I, \Theta)$  in phase space at final time  $t_f$  for  $n=1, 2, 3$  chirped frequency drives. One can see three separated resonant buckets centered at final resonant actions  $I_r = 1.00, 0.75, 0.50$ . The nearly uniform color of each bucket indicates the origin of the trapped electrons, i.e., from the vicinity of initial resonances at  $I = 2.50, 1.25, 0.83$ , respectively. The single resonance approximation is expected to work in this case.

sponding resonance. Still, because of the separation of the resonant regions, the single resonance approximation could be used to treat each of these resonances separately. We compare these results with a similar simulation [shown in Figs. 10, 11(a), and 11(b)], where the driving amplitudes are increased to  $\varepsilon_{1,2,3} = 0.01$ . The distance between  $n=2$  and  $n=3$  resonances (0.25 in this case) is nearly the same as the averaged width of the resonances and one expects to see some of the  $n=2$  and  $n=3$  overlap effects. Indeed, in Fig. 10 we still observe a well-defined  $n=1$  bucket in phase space. Only a residual  $n=2$  bucket can be seen, while the neighboring  $n$

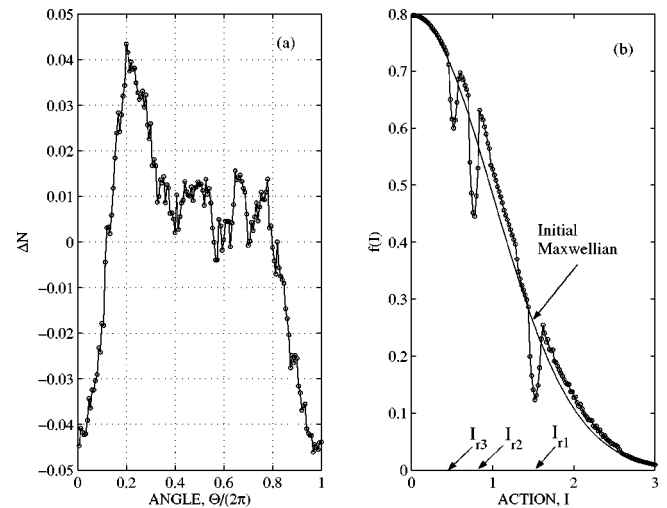


FIG. 9. The angle/space averaged distributions for a three-mode drive. The driving amplitudes are  $\varepsilon_n = 0.003$ ,  $n=1, 2, 3$ . (a) The normalized electron density perturbation  $\Delta N$  (circles) vs angle; (b) The space-averaged electron distribution function  $f$  vs  $I$  (circles) at  $t = t_f$ . The initial Maxwellian distribution is shown for comparison. The characteristic local depressions in the driven distribution have the minima located, as expected, at the exact resonances  $I = I_r^{(n)}$ .

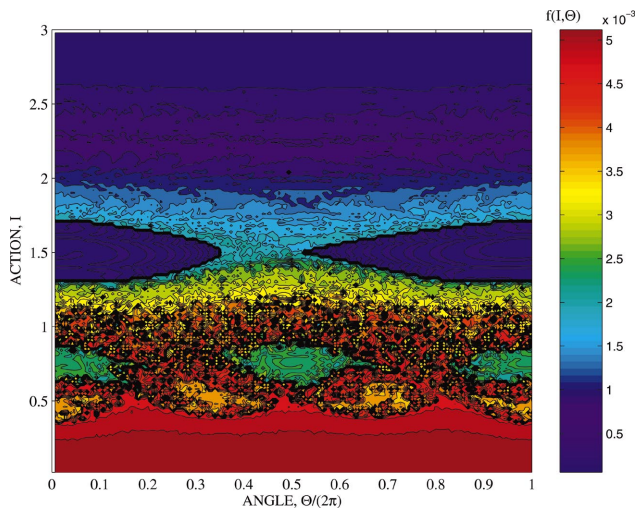


FIG. 10. (Color). The color map of the electron distribution  $f(I, \Theta)$  in phase space at final time  $t_f$  for combined  $n=1, 2, 3$  chirped frequency drives. The parameters are the same as in Fig. 8, but all three driving amplitudes are increased to  $\varepsilon_n=0.01$ . One can see the well separated  $n=1$  resonant bucket, while the boundary of  $n=2$  bucket is largely deformed, while  $n=3$  bucket nearly disappears due to interaction of resonances. The single resonance approximation in this case is not applicable for treating  $n=2, 3$  resonances.

$=3$  bucket nearly disappears. A similar effect is seen in the distribution function in Fig. 11(b); the normalized density perturbation  $\Delta N$  in Fig. 11(a) is larger than that in Fig. 9(a), mostly because of the larger  $n=1$  driving amplitude.

Finally, we compare the Fourier spectra of the induced density perturbations  $\Delta N(\Theta)$  at different driving conditions in Figs. 12(a)–12(c). The spectrum in the case of a single frequency drive, for the small driving amplitude conditions of Figs. 5 and 6, is shown in Fig. 12(a). An almost purely  $n=1$  response is seen. Figure 12(b) shows the spectrum for small amplitude, three-component ( $n=1, 2, 3$ ) drive with nonoverlapping resonances. The parameters are as those of

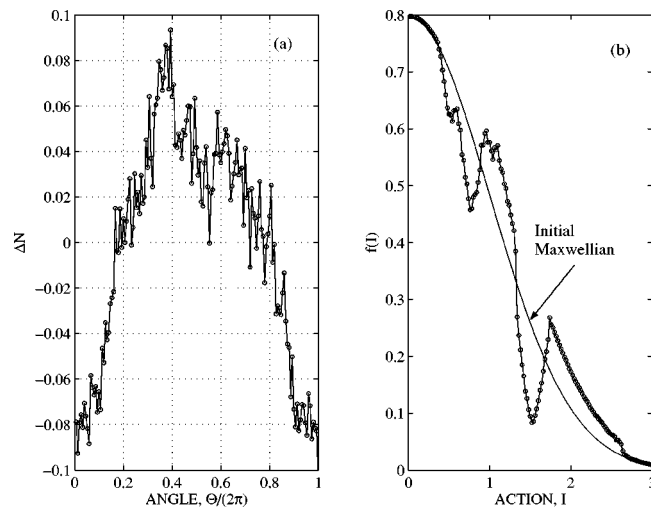


FIG. 11. The angle/space averaged distributions for the case shown in Fig. 10. (a) The normalized electron density perturbation  $\Delta N$  (circles) versus angle. (b) The space-averaged electron distribution function  $\bar{f}$  vs  $I$  (circles) at  $t=t_f$ . The characteristic  $n=2, 3$  local depressions are strongly affected by interaction of resonances as compared to the lower driving amplitude case shown in Fig. 9.

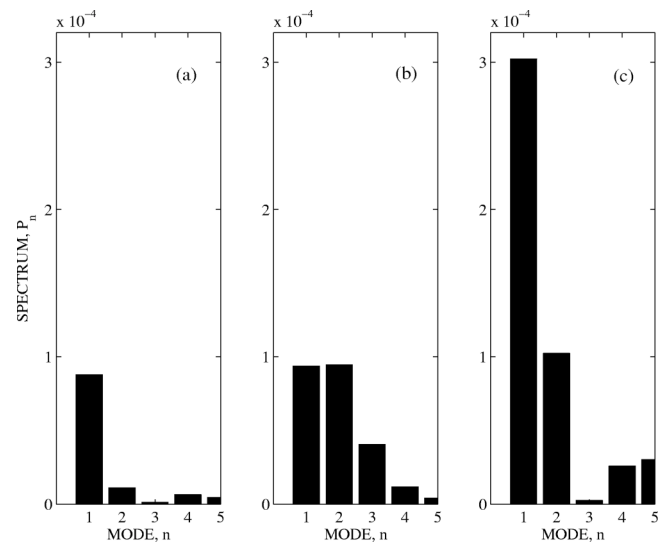


FIG. 12. The comparison of the Fourier spectra,  $P_n$  of the electron density perturbations induced by a chirped frequency drive. (a) Small amplitude, single  $n=1$  mode drive. The parameters are as those in Figs. 5 and 6. An almost purely  $n=1$  response is seen. (b) Small amplitude three-component ( $n=1, 2, 3$ ) drive with non-overlapping resonances. The parameters are as those in Figs. 8 and 9. The response consists mostly of three nearly independent modes. (c) Larger amplitude three-component drive with overlapping  $n=2, 3$  resonances. The parameters are as those in Figs. 10 and 11. Only the  $n=1$  driven component grows significantly as compared to (b), while the  $n=2$  response remains nearly the same and the  $n=3$  response practically disappears due to the resonance overlap.

Figs. 8 and 9. The single resonance approximation is valid and the response consists primarily of three nearly independent modes. In contrast, Fig. 12(c) shows the case of a larger amplitude three-component drive with overlapping  $n=2, 3$  resonances. The parameters are as in Figs. 10 and 11. Only an  $n=1$  driven component grows significantly as compared to Fig. 12(b), while the  $n=2$  response remains nearly the same and the  $n=3$  response practically disappears, due to the resonance overlap. This completes our analysis of a driven Maxwellian plasma dynamics with a prescribed chirped frequency drive, but neglecting the self-field. We now proceed to add the latter to our model.

### III. CHIRPED-BUCKET BGK MODES

Here, we extend our driven,  $1D$ , trapped electron plasma model, by including the interaction with a more general potential perturbation  $\nu(z, t) = \varphi[z, \psi(t), t] + \varphi_d[z, \psi_d(t), t]$ , that includes both the driving,  $\varphi_d$ , and the self-field,  $\varphi$ , components. We use a two-time-scale representation of the potentials, i.e., view  $\varphi$  and  $\varphi_d$  as  $2\pi$ -periodic functions of *fast* phase variables  $\psi$  and  $\psi_d$ , respectively, but, at the same time, assume that the frequencies  $\omega(t) = d\psi/dt$  and  $\omega_d(t) = d\psi_d/dt$  are slow functions of time. The explicit time dependence in  $\varphi[z, \psi(t), t]$  is also assumed to be slow. We recall that, by the nature of emergence of the resonant buckets in phase space in our model in Sec. II, their phases and the phases of the corresponding induced density perturbations were the same as of the driving field. We shall assume a similar situation when one includes the slowly varying self-potential as a part of the driving perturbation. In other words,

we assume that the phase mismatch  $\phi = \psi(t) - \psi_d(t)$  is both small and slow at all times, despite the variation of the driving frequency. The electron dynamics are now governed by the Hamiltonian

$$H(p, z, t) = \frac{p^2}{2m} - e\nu(z, t), 0 \leq z \leq L. \quad (11)$$

We again transform to the action-angle variables,  $(I, \theta)$ , of the unperturbed problem (see Sec. II). The transformed Hamiltonian is

$$H(I, \theta, t) = \frac{1}{2}\mu I^2 - e\nu[z(\theta), t].$$

We expand  $\nu$  in the last equation in a Fourier series in  $\theta$ . By definition, both  $\varphi$  and  $\varphi_d$  are symmetric around  $\pi$  with respect to  $\theta$  and, therefore, we have

$$\varphi = \sum_n f_n(\psi, t) \cos(n\theta); \quad \varphi_d = \sum_n g_n(\psi_d) \cos(n\theta).$$

Next, we use  $2\pi$  periodicity with respect to  $\psi, \psi_d$ , to expand  $f_n$  and  $g_n$  in a Fourier series, and, by focusing on a single mode interaction, leave only the combination of  $n$ th  $\theta$  harmonic and first  $\psi, \psi_d$  harmonics in  $e\nu$  in the Hamiltonian, obtaining [compare to Eq. (3)]

$$H_n = \frac{1}{2}I^2 - 2[a_n(t) \cos \psi(t) + \varepsilon_n \cos \psi_d(t)] \cos(n\theta). \quad (12)$$

Here  $a_n(t)$  and  $\varepsilon_n$  are real amplitudes of generally complex, driven, and driving Fourier coefficients, respectively; the complex phases of the amplitudes are absorbed in the definitions of  $\psi$  and  $\psi_d$ . We shall assume that  $\varepsilon_n > 0$ , but allow both positive and negative signs of  $a_n(t)$  (see below). Also, in Eq. (12), we again use dimensionless variables and parameters [ $t \rightarrow \Omega_{th} t$ ,  $I \rightarrow I/I_{th}$ ,  $\omega_d \rightarrow \omega_d/\Omega_{th}$ ,  $\varepsilon_n \rightarrow \varepsilon_n/(m\nu_{th}^2)$ , and  $a_n \rightarrow a_n/(m\nu_{th}^2)$ , where  $\Omega_{th} = \pi v_{th}/L$  and  $I_{th} = mLv_{th}/\pi$  (see Sec. II)]. Other resonances can be treated independently by similar Hamiltonians, as long as both the driving and the self-field amplitudes remain small and the resonances do not overlap, as described in Sec. II.

The Hamiltonian (12) will be used in our kinetic theory below [starting Eq. (14)]. The theory will describe the effect of the resonant particles on the excited wave, but also include the driven response (i.e., the response at the driving frequency) of the nonresonant part of the distribution. The latter contributes, via the principal value integral  $G$ , in our final result [see Eq. (29) below]. Thus, the interaction of the wave with the whole thermal distribution will be included in our kinetic model. At the same time, the dynamics of the resonant particles is easier to understand on the basis of our discussion in Sec. II. Indeed, the resonant particles can be described by a simplified, *single resonance* Hamiltonian obtained from Eq. (12), under the phase-locking assumption  $\psi \approx \psi_d$

$$H'_n \approx \frac{1}{2}I^2 - [a_n(t) + \varepsilon_n] \cos(n\theta - \psi_d), \quad (13)$$

which is similar to Eq. (4), but the slowly varying amplitude,  $\varepsilon'_n(t) = a_n(t) + \varepsilon_n$ , now includes the self-component  $a_n(t)$  (to be evaluated later). Therefore, we expect the dynamics governed by Eq. (13) to be similar to that described in Sec. II. For example, if  $a_n(t)$  grows slowly with time, as the driving

frequency decreases, all the electrons initially trapped in the resonant bucket remain trapped at later times and some new particles will be added to the resonant group, as the bucket drifts towards the bulk of the distribution. This will create a local depression (hole) in the phase space, that oscillates in  $\Theta = \text{mod}(\theta, 2\pi)$  and slowly drifts in  $I$ . The hole, in turn, yields the electron density perturbation, which is phase locked to the drive, and the appearance of the characteristic minimum in the space-averaged electron velocity distribution. This situation is similar to the growing driving amplitude example in Figs. 7(a) and 7(b).

At this stage, we proceed to our kinetic theory. Let  $f(I, \theta, t)$  be the distribution of the electrons in  $(I, \theta)$  space. The distribution is described by the Vlasov equation

$$\frac{\partial f}{\partial t} + I \frac{\partial f}{\partial \theta} - 2n(a_n \cos \psi + \varepsilon_n \cos \psi_d) \sin(n\theta) \frac{\partial f}{\partial I} = 0, \quad (14)$$

where Hamiltonian (12) is used in the equations of motion

$$d\theta/dt = I$$

$$dI/dt = -2n(a_n \cos \psi + \varepsilon_n \cos \psi_d) \sin(n\theta).$$

Recall that, by definition of the angle variable, both  $\Theta = \text{mod}(\theta, 2\pi)$  and  $2\pi - \Theta$  correspond to the same position  $z$  in configuration space. Consequently, we normalize our distribution so that, for a given  $\Theta = \pi z/L$ ,  $z \in [0, L]$ , the integral

$$\int_0^{+\infty} [f(I, \Theta, t) + f(I, 2\pi - \Theta, t)] dI = \frac{n(z, t)}{n_0} \quad (15)$$

is the normalized electron density at  $z$ ,  $n_0$  being the initial (unperturbed) density.

We seek phase-locked solutions of Eq. (14) in the form  $f = F[I, \theta, \psi(t), t]$ , where  $F$  is  $2\pi$  periodic in both  $\theta$  and  $\psi$ , while, as before,  $d\psi/dt$  and the explicit dependence on  $t$  in  $F$  are slow. Then, expansion in a double Fourier series yields

$$F(I, \theta, t) = \sum_{n, m=-\infty}^{\infty} C_{n, m}(I, t) \exp[i(n\theta - m\psi)], \quad (16)$$

where  $C_{n, m}(I, t) = C_{-n, -m}^*(I, t)$  vary slowly. Finally, in studying slow resonant excitations of a specific  $n$ th  $\theta$  harmonic of the distribution, we drop all the terms in Eq. (16) but the  $\theta, \psi_d$ -averaged term, and those with phases  $n\theta \pm \psi$ , i.e., we write

$$F(I, \theta, t) \approx \bar{f}(I, t) + (A_n e^{i\psi_d} + B_n e^{-i\psi_d}) e^{in\theta} + \text{c.c.}, \quad (17)$$

where the slow factors  $e^{\pm i\phi}$  are included in  $A_n$  and  $B_n$ . Note that  $\bar{f}(I, t)$  in this expression is the space-averaged distribution of actions (velocities); it may have a nonperturbative [ $O(1)$ ] local depression, when compared to the initial Maxwellian distribution (see the discussion in Sec. II). As the result,  $A_n, B_n$  in Eq. (17) may not be necessarily small (see below) and, consequently, we do not view Eq. (17) as a perturbation expansion, but rather expansion of the distribution function in harmonics. At the same time, the amplitudes  $a_n$  and  $\varepsilon_n$  are still viewed as small perturbations. We substitute Eq. (17) into Eq. (14) and collect the coefficients of terms with  $\exp[i(n\theta \pm \psi_d)]$ , yielding

$$\frac{\partial A_n}{\partial t} + i(nI + \omega_d)A_n + \frac{in}{2}(a_n e^{i\phi} + \varepsilon_n) \frac{\partial \bar{f}}{\partial I} = 0, \quad (18)$$

$$\frac{\partial B_n}{\partial t} + i(nI - \omega_d)B_n + \frac{in}{2}(a_n e^{-i\phi} + \varepsilon_n) \frac{\partial \bar{f}}{\partial I} = 0, \quad (19)$$

where, as before,  $\phi = \psi - \psi_d$  is the phase mismatch.

Now, we write the Poisson equation for the induced, dimensionless, self-potential,  $e\varphi/mv_{th}^2$ ,

$$\left( \frac{\partial^2}{\partial z^2} - \kappa^2 \right) \left( \frac{e\varphi}{mv_{th}^2} \right) = \lambda_D^{-2} \frac{\Delta n(z)}{n_0}. \quad (20)$$

Here, parameter  $\kappa$  (as before) models the inverse radial scale of the mode excited in our bounded, small aspect ratio ( $R/L \ll 1$ ) plasma,  $\lambda_D = v_{th}/\omega_p$  is the Debye length,  $\omega_p = (4\pi e^2 n_0/m)^{1/2}$  is the plasma frequency, and  $\Delta n(z)/n_0$  is the normalized, *oscillating* component of the electron density perturbation. The latter is calculated from Eq. (15),

$$\frac{\Delta n(z)}{n_0} = \int_0^{+\infty} \{ [F(I, \Theta, t) - \bar{f}] + [F(I, 2\pi - \Theta, t) - \bar{f}] \} dI. \quad (21)$$

By substituting Eq. (17) into Eq. (21), using the result in the Poisson Eq. (20), where  $\partial^2/\partial z^2 = (\pi/L)^2 \partial^2/\partial \Theta^2$ , and collecting the terms with  $\exp[i(n\Theta - \psi_d)]$ , we find

$$a_n e^{-i\phi} = -2p^2 \int_0^{+\infty} (B_n + A_n^*) dI, \quad (22)$$

where  $a_n$  is the amplitude of the induced  $e\varphi$  component [see Eq. (12)],  $p = (\kappa \lambda_D \mu)^{-1}$ , and  $\mu^2 = 1 + (n\pi/\kappa L)^2$ . Equations (18), (19), and (22) comprise the desired, closed set of three complex equations for  $A_n$ ,  $B_n$ , and  $a_n e^{i\phi}$ . We now proceed to the solution of these equations.

We associate a slow BGK mode in our system with the (*quasistatic*) solution of Eqs. (18) and (19), where one neglects  $\partial B_n/\partial t$  and  $\partial A_n/\partial t$ . This yields  $\phi \equiv 0$  (perfect phase locking) and purely real amplitudes

$$A_n \approx - \frac{n\varepsilon'_n}{2(nI + \omega_d)} \frac{\partial \bar{f}}{\partial I}, \quad B_n \approx - \frac{n\varepsilon'_n}{2(nI - \omega_d)} \frac{\partial \bar{f}}{\partial I}, \quad (23)$$

$$a_n = -2p^2 \int_0^{+\infty} (B_n + A_n) dI, \quad (24)$$

where, as before,  $\varepsilon'_n = a_n + \varepsilon_n$ . Equations (23) show that the quasistatic approximation is valid, provided the time variation of  $\omega_d$  and  $\varepsilon'_n$  is sufficiently slow. The resonant form of  $B_n$  at  $nI = \omega_d$  does not change this conclusion, as will be explained shortly. Next, we use  $\bar{f}$  with a parabolic localized depression in the resonant region illustrated in the examples in Sec. II. In other words, to lowest order, we assume that outside the resonant bucket ( $|I - \omega_d/n| > \Delta I$ ),  $\bar{f}$  coincides with the unperturbed normalized distribution  $\bar{f} = f_0(I)$ , while inside the bucket ( $|I - \omega_d/n| < \Delta I$ ) [compare to Eq. (8)]

$$\bar{f}(I, t) \approx f_0\left(\frac{\omega_d}{n}\right) - h + \frac{h}{\Delta I^2} \left( I - \frac{\omega_d}{n} \right)^2 \quad (25)$$

with the slow time dependence entering via  $\omega_d$ ,  $h$ , and  $\Delta I$ . Then,

$$A_n = - \frac{n\varepsilon'_n}{2(nI + \omega_d)} \frac{\partial f_0}{\partial I}, \quad B_n = - \frac{n\varepsilon'_n}{2(nI - \omega_d)} \frac{\partial f_0}{\partial I}, \quad (26)$$

and

$$A_n = - \frac{\varepsilon'_n h (nI - \omega_d)}{\Delta I^2 (nI + \omega_d)}, \quad B_n = - \frac{\varepsilon'_n h}{\Delta I^2}, \quad (27)$$

outside and inside the resonant region, respectively. Since  $\Delta I$  is of  $O(\varepsilon_n'^{1/2})$ , outside the bucket,  $A_n$  and  $B_n$  are of  $O(\varepsilon_n')$ . In contrast, inside the resonant region,  $A_n$  is of  $O(\varepsilon_n'^{1/2})$ ,  $B_n$  scales as  $O(h)$  and may be  $O(1)$ , but both  $A_n$  and  $B_n$  remain slow. The nonperturbative scaling of the driven, quasistatic response in the bucket region is the important signature of the resonant interaction in our driven problem.

Now, it remains to perform integration in the right-hand side (RHS) in Eq. (24). We use Eqs. (26) and (27) and assume a small width of the resonant bucket, i.e. (in dimensionless units),  $\Delta I \ll 1$ . Then, the integral in the RHS in Eq. (24) can be approximated by

$$\begin{aligned} P \int_0^{+\infty} \frac{\partial f_0(\varepsilon'_n/2) dI}{\partial I I - \omega_d/n} + \int_0^{+\infty} \frac{\partial f_0(\varepsilon'_n/2) dI}{\partial I I + \omega_d/n} + \frac{2h\varepsilon'_n}{\Delta I} \\ = \frac{\varepsilon'_n}{2} \left( P \int_{-\infty}^{+\infty} \frac{\partial f'_0}{\partial I I - \omega_d/n} \frac{dI}{\Delta I} + \frac{4h}{\Delta I} \right), \end{aligned}$$

where  $P(\dots)$  denotes the usual principal value integration,  $f'_0$  is the symmetric extension of  $f_0$  to both negative and positive  $I$ , i.e.,  $f'_0(-I) = f'_0(I) = f_0(I)$ , and, by our normalization,  $\int_{-\infty}^{+\infty} f'_0 dI = 1$ . If we specialize<sup>16</sup> to a Maxwellian,  $f'_0 = (2\pi)^{-1/2} \exp(-I^2/2)$ ,

$$P \int_{-\infty}^{+\infty} \frac{(\partial f'_0/\partial I) dI}{I - \omega_d/n} = 2\xi S(\xi) - 1 \equiv G(\xi), \quad (28)$$

where  $S(\xi) = 1/4[Z(-\xi) - Z(\xi)]$ ,  $\xi = \omega_d/(\sqrt{2}n)$ , and  $Z(\xi)$  is the usual plasma dispersion function. Importantly, the function  $G(\xi)$  has a single maximum:  $G_m = 0.28$  at  $\xi_m \approx 1.5$ , i.e., at  $\omega_d = 2.12\Omega_{th}$ , while asymptotically, at large  $\xi$ ,  $G(\xi) \approx 1/2\xi^2$ .<sup>16</sup> The substitution of Eq. (28) into Eq. (24) yields the desired expression for the amplitude of the induced field,

$$a_n = p^2 \left[ \frac{4h}{\Delta I} + G(\xi) \right] \varepsilon'_n. \quad (29)$$

We recall that  $\varepsilon'_n = a_n + \varepsilon_n$ , and, in the limit  $\alpha \ll \varepsilon'_n$ ,  $n\Delta I = 2\sqrt{|\varepsilon'_n|}$ . Then Eq. (29) becomes a quadratic equation for  $\sqrt{|\varepsilon'_n|}$ ,

$$sR(\xi)|\varepsilon'_n| - 2nhp^2 s\sqrt{|\varepsilon'_n|} - \varepsilon_n = 0, \quad (30)$$

where  $s = \text{sign}(\varepsilon'_n)$  and  $R(\xi) = 1 - p^2 G$ . This equation yields a multiplicity of physical (positive) solutions, which can be classified depending on the sign  $s$  of the total field amplitude  $\varepsilon'_n$  (the driving amplitude  $\varepsilon_n$  is assumed to be positive). If

$s > 0$ ,  $R$  must be positive and the corresponding solution is (type-I solution in the following):

$$\sqrt{|\varepsilon'_n|} = \frac{nhp^2}{R} + \sqrt{\frac{n^2h^2p^4}{R^2} + \frac{\varepsilon_n}{R}}, \quad R > 0. \quad (31)$$

In contrast, for  $s < 0$  (both  $\varepsilon'_n$  and  $a_n$  are negative in this case), there exist three solutions (type-II, -III, and -IV solutions, respectively) depending on the sign of  $R$ ,

$$\sqrt{|\varepsilon'_n|} = -\frac{nhp^2}{|R|} + \sqrt{\frac{n^2h^2p^4}{R^2} + \frac{\varepsilon_n}{|R|}}, \quad R < 0, \quad (32)$$

$$\sqrt{|\varepsilon'_n|} = \frac{nhp^2}{R} \pm \sqrt{\frac{n^2h^2p^4}{R^2} - \frac{\varepsilon_n}{R}}, \quad R > 0. \quad (33)$$

Note that type-I and -II solutions exist in case  $h < 0$  (a clump instead of a hole in the distribution, see below), while solutions III and IV become unphysical in this case. Also, only type-I and -II solutions above are allowed for  $h=0$  and finite  $\varepsilon_n$ . Therefore, only these two solutions are of interest in our system, where  $h$  develops, starting from zero, as the result of a slow drift of the resonant bucket in phase space. Consequently, we shall not discuss further excitations of type III and IV.

Now, we consider several limits of Eqs. (31) and (32). Suppose, at  $t=0$ , the driving frequency resonates in the tail of the initial distribution, i.e.,  $\xi \gg 1$ ,  $p^2G < 1$  (i.e.,  $R > 0$ ) and  $h \approx 0$ . Then, initially, we proceed from type-I solution, the driven response is  $a_n \approx p^2G(\xi)\varepsilon_n \approx \varepsilon_n/(\kappa\lambda_D\mu\xi)^2$ , and the self-field amplitude growth starts due to the decrease of  $\xi$ , as the driving frequency chirps down. At later times, the depth  $h$  of the depression in the space-averaged distribution function increases, which contributes to additional growth of  $a_n$  via the terms with  $nhp^2/R$  in Eq. (31). These terms may become dominant if the resonant bucket approaches the bulk of the distribution, where  $h$  is of  $O(1)$ . Then, Eq. (31) yields

$$\sqrt{\varepsilon'_n} \approx \frac{2nhp^2}{R(\xi)}. \quad (34)$$

Because of the characteristic form of function  $R(\xi)$ , having a single minimum,  $R_m = 1 - p^2G_m$ , the dependence of  $a_n$  on time in Eqs. (31) and (34) with the decrease of the driving frequency is different for  $p^2G_m < 1$  and  $p^2G_m > 1$ . The extreme latter case,  $p^2 \gg 1$ , is the cold plasma limit. In this case,  $R(\xi)$  passes through zero at some  $\xi_0 \gg 1$  and then becomes negative. Then, only a type-II solution is allowed. This means rapid variation of the amplitude near  $\xi_0$  and a discontinuity in the solution at  $\xi_0$ , i.e., violation of adiabaticity. The plasma cannot support a quasistatic, synchronized BGK mode for  $\xi \lesssim \xi_0$  in this case and the phase locking with the drive is expected to be lost. Since, prior reaching  $\xi_0$ , the resonant bucket is still in the tail of the distribution,  $h$  in Eq. (31) is exponentially small, and, consequently, no significant driven response is expected in the cold plasma limit. Another case corresponds to  $p^2G_m > 1$  (still sufficiently cold plasma case), but, initially, at  $t=0$ ,  $R < 0$ . Then, a type-II solution characterized by negative self-field amplitude is excited initially, and, as we approach  $\xi_0$  [recall that  $R(\xi_0)=0$ ], Eq. (32) yields

a solution with a *decreasing* amplitude  $\sqrt{|\varepsilon'_n|} \approx \varepsilon_n|R|/nhp^2$ . Therefore, no large excitation is expected in this case as well.

A very different scenario characterizes sufficiently hot plasmas, where  $p^2G_m < 1$ . Then,  $R > 0$  for all  $\xi$  and we excite a type-I solution without encountering a discontinuity in the process of evolution. The phase-locking persists as the driven bucket approaches the bulk of the distribution. A large driven response is expected, as function  $R(\xi)$  in Eq. (34) passes a minimum at  $\xi_m \approx 1.5$ , i.e., at  $\omega_d \approx 2.1\Omega_{th}$ . If  $h$  continues to increase with the decrease of the driving frequency, the actual maximum value of  $a_n$  is expected at  $\xi < \xi_m$ . Also, the largest driven response in this scenario is expected for  $p^2G_m$  close to unity. Finally, in the hot plasma case ( $p^2G_m < 1$ ), a clump ( $h < 0$ ) instead of a hole can be created by first resonating in the bulk of the distribution and then moving to the tail by slowly upshifting the driving frequency. Since  $R > 0$  in this case, we excite type-I solution (31). If, as we approach the tail of the distribution, where  $R \approx 1$ , we have  $n^2h^2p^4/R \leq \varepsilon_n$ , Eq. (32) yields a small solution  $\sqrt{|a_n|} \approx \varepsilon_n/n|h|p^2$ . Physically, the associated self-field in the clump case cancels that of the drive and no large excitation can emerge from an upshifted frequency drive.

These predictions agree well with the results of our experiments.<sup>13</sup> For example, in Fig. 3, showing the response to chirped frequency drive at  $T_e = 6$  eV, one observes multiple maxima of the driven response at  $\omega_d \approx 1.3n\Omega_{th}$ . In these experiments,  $T_e = 6$  eV,  $\omega_p = 1.7 \times 10^8 \text{ s}^{-1}$ ,  $\kappa \approx 1 \text{ cm}^{-1}$ , and one finds  $p^2G_m \approx 0.8$ , close to the expected condition for having the largest amplitude, driven bucket-BGK modes. If, in contrast,  $T_e = 1$  eV, we find  $p^2G_m \approx 5$ ,  $\xi_0 \approx 3.5$  and, depending on the initial value of  $\xi$ , one expects either a dephasing of the driven type-I solution at  $\xi_0$  (if, initially,  $\xi > \xi_0$ ), still being in the tail of the distribution, or a decreasing type-II solution (if, initially,  $\xi < \xi_0$ ) as explained above. Therefore, no large driven response is expected at this temperature, as confirmed in experiments.<sup>13</sup> Finally, if at large type-I excitations, when  $a_n \gg \varepsilon_n$ , we switch off the driving field, the remaining wave form will be just slightly different from its final state with the drive and, therefore, it will continue to support itself via the resonant bucket, associated with the self-field only. In this case,  $\omega_d$  in Eq. (34) becomes the frequency  $\omega$  of the excited wave and we interpret this equation as the dispersion relation of the free BGK mode. The reality of  $\omega$  in the dispersion indicates stability of the excited wave, as, indeed, has been observed in experiments, where  $Q$  factors of up to 100 000 have been measured, after switching off the driving field. It should be also mentioned that other phenomena, such as resonance overlap, nonlinear interactions between modes with different mode numbers, dephasing and flattening of the local minimum in the distribution due to a faster growth of the excited wave, and three-dimensional effects may affect the finite excitation amplitudes of driven, chirped-bucket BGK modes.

Next, we proceed to self-consistent particle-in-cell (PIC) simulations, focusing on testing predictions of our small amplitude theory, and visualizing large amplitude excitations for comparison with experiments. We postpone a more detailed numerical and analytical study of the aforementioned nonlin-

ear phenomena and three-dimensional effects associated with synchronized BGK modes to future work.

#### IV. PIC SIMULATIONS

Our one-dimensional simulations assume an initially uniform electron density in the trap. Such a density profile is not in equilibrium with the self-consistent potential, leading to density spikes at the ends of the plasma column during the evolution. This limits the precision of description in the end regions. We have also assumed a square well shape for the confining potential, defined by edge electrodes. Despite of all these simplifications, interesting results have been obtained, confirming main predictions of the small amplitude theory and yielding very good qualitative agreement with the experimental results at large excitations. Nonetheless, in the future, simulations based on a more accurate model will be performed, using more realistic profiles for both the confining and drive potentials, allowing detailed quantitative comparisons with experimental results.

We used a standard, 1D, electrostatic PIC code<sup>17</sup> in the simulations. A modified Poisson equation has been solved in  $z$  space ( $z, v_z$  coordinates have been used in the code) with the boundary conditions defined by assuming an exponential decay of the potential at the ends of the trap with a characteristic inverse decay length  $\kappa$ . We used a value for  $\kappa$  as given by the radial scale in the problem, the latter found by expanding the self-consistent potential in Fourier-Bessel series and retaining only the first term in the series. Therefore,  $\kappa$  has been set to  $j_{01}/R_{trap}$ , where  $j_{01}$  is the first zero of  $J_0$  Bessel function and  $R_{trap} \approx 2$  cm is the radius of the trap. With these assumptions,  $\kappa \approx 1.2 \text{ cm}^{-1}$ . The confining square well potential has been taken into account in the definition of the suitable boundary conditions for the Poisson equation and in the particle mover, by imposing elastic collisions against the potential wall for the particles reaching the ends of the plasma column. We have assumed the plasma length of 30 cm,  $\omega_p = 1.7 \times 10^8 \text{ s}^{-1}$ , and two different values of the temperature,  $T_{e,1} = 6 \text{ eV}$  (hot plasma case) and  $T_{e,2} = 1 \text{ eV}$  (cold plasma case). In all our simulations below (as in previous sections), the dimensionless sweep rate has been set to  $\alpha = 0.001$  and the dimensionless drive frequency  $\omega_d$  has been swept from 2.5 to 1.5. Only the first harmonic of the driving potential has been included, although, a higher harmonic content could be easily introduced in the code, and nearly 50 000 computational particles have been employed.

The numerical results in Sec. II, where we neglected the self-field (see Fig. 5), predict the formation of a hole in the phase space (the separatrix can be clearly identified in the figure) which extends to nearly all of the plasma column, and is relatively narrow in velocity, because of the small driving amplitude. For this reason, the oscillating hole does not yield large density oscillations (see Fig. 6). Furthermore, these non-self-consistent results are independent of the plasma temperature, which scales out in the dimensionless formulation. In contrast, when the self-field is included, the temperature enters explicitly in the dimensionless model via the debye length in the source term of Poisson equation [see Eq. (20)]. This important difference leads to very different dy-

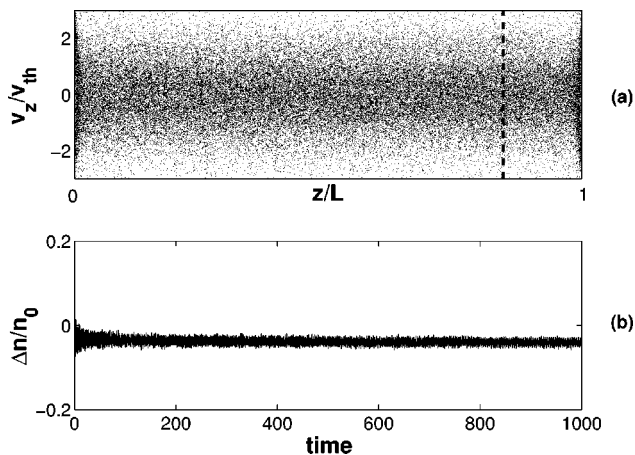


FIG. 13. (a) Phase-space portrait of the system at the end of the evolution, for  $\varepsilon_1=0.017$ ,  $\alpha=0.001$  and  $T_e=1 \text{ eV}$ . (b) Time evolution of the plasma density at the point marked by a dashed line in (a).

namics for hot and cold plasmas. Figures 13(a) and 13(b) show the results of a simulation run in the cold plasma case and dimensionless drive amplitude  $\varepsilon_1=0.017$ : Fig. 13(a) is the phase-space portrait of the plasma at the final time of excitation, while Fig. 14(b) plots the time evolution of the density perturbation (normalized to the initial density  $n_0$ ) at position  $z_0$  marked by the dashed line in Fig. 14(a). Figure 13(b) clearly shows that the cold plasma response remains small throughout the excitation process. The normalized amplitude of the density perturbation reaches a maximum of  $\approx 1\%$  in the initial stage of excitation, where the bucket is still in the tail of the distribution, and then decreases in time, almost disappearing at the final time of simulations, as discussed at the end of Sec. III, for a type-II solution with nearly the same cold plasma parameters. No significant difference in the results have been observed at higher driving amplitudes, the density perturbation always decreased in time. The absence of large excitations in 1 eV plasmas was also confirmed in experiments.<sup>13</sup>

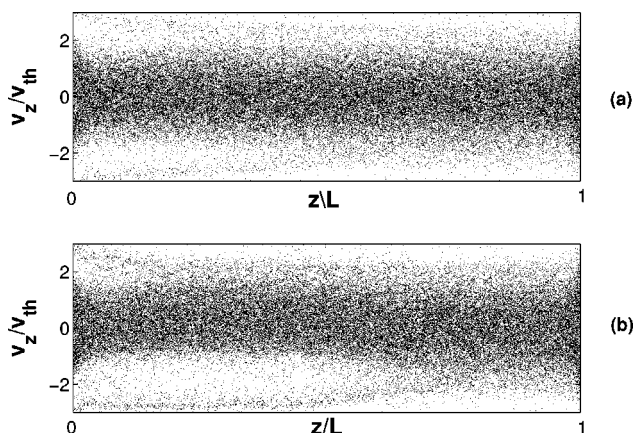


FIG. 14. Phase-space portraits of the system at one third (a) and at two thirds (b) of the chirped-frequency driving process, for  $\varepsilon_1=0.017$ ,  $\alpha=0.001$  and  $T_e=6 \text{ eV}$ .

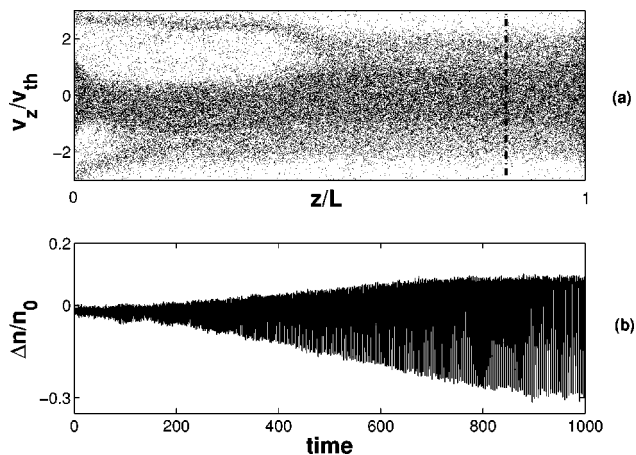


FIG. 15. (a) Phase-space portrait of the system at the end of the evolution for all parameters as in Fig. 14. (b) Time evolution of the plasma density at the point marked by a dashed line in (a).

A very different response was found in simulations for 6 eV plasma case. The self-consistent evolution at this temperature is illustrated in Figs. 14(a) and 14(b) and Figs. 15(a) and 15(b), for the same dimensionless drive amplitude and other parameters and initial conditions as in the cold plasma case. The effect of the temperature on the evolution of the perturbed density is evident: the system response grows continually in time, reaching very large amplitudes at the end of the excitation process. The initial growth of the amplitude in this case corresponds to the growing type-I solution, discussed for similar plasma parameters at the end of Sec. III. The amplitude of the oscillating part of the relative electron density perturbation in the small amplitude limit can be found from Eq. (20) in our theory, i.e.,  $\Delta n/n_0 = a_1/p^2$ . Here, for large excitations,  $a_1 \approx \varepsilon'_1$ , and, therefore, substituting Eq. (34), one finds  $\Delta n/n_0 = 4h^2 p^2/R^2$ . For simulations parameters in the hot plasma case,  $p^2 = 2.1$ ,  $h$  can be estimated as 0.1, and  $R \approx 0.75$  ( $\xi \approx 1.06$ ) at the final time of the simulation. This yields the amplitude  $\Delta n/n_0 = 0.15$ , which must be viewed only as an estimate, because small amplitude assumption is violated at the final time. Still, our estimate and simulations are in a good agreement [see Fig. 15(b)].

The evolution of the phase space portrait of the plasma as shown in Figs. 14 and 15 provides another visualization of the effect of the self-field on the process of formation and development of the resonant bucket. In the self-consistent case, one observes that the low density bucket region becomes increasingly wide in velocity space, but, at the same time, is confined to a smaller, well-defined part of the plasma length, as it should be due to the conservation of the total area of the low density region in phase space. This spatial localization of the bucket at large excitations results in a higher spatial harmonic content of the self-field, as observed in experiments. The growing width of the bucket in the velocity space also yields large modulations in the plasma density, with relative density variations reaching 20%–30%, as shown in Fig. 15(b). Similar size excitations have been also observed in experiments at analogous conditions<sup>13</sup> (see Fig. 3).

## V. CONCLUSIONS

- (a) We have studied the emergence and control of BGK-type modes in trapped pure electron plasmas. The goal was achieved by applying an oscillating, external driving potential with a slowly down-chirped frequency and exploiting the transient bounce-resonance phenomenon with the electrons in the trap. Initially, the drive resonates with a group of electrons in the tail of the distribution function. Some of these electrons are trapped in resonance and remain trapped despite variation of the driving frequency, while some new electrons are added to the resonant bucket as it slowly drifts with the decrease of the driving frequency, towards lower resonant velocities. Since most of the resonantly trapped electrons belong to the tail of the electron velocity distribution, their density is low compared to that of untrapped particles, as the bucket approaches the bulk of the distribution. The excited, chirped-bucket BGK modes are associated with this synchronized, low density depression (hole) in phase space.
- (b) To develop our intuition and demonstrate the effects of the chirped frequency drive on the resonant bucket dynamics, we started our analysis with simplified simulations, while neglecting the self-field. The simulations provided us with the electron distribution function in phase space, within this approximation, and illustrated the emergence of a growing depth hole in the distribution, as the driving frequency was chirped down. It was also shown that the corresponding, space-averaged distribution of the electrons developed a characteristic depression, having the width of the resonant bucket in the velocity space. The minimum of this depression was located at the slowly drifting position of the exact bounce-resonance, and its relative depth could become large,  $O(1)$ , as the resonant bucket travels from the tail to the bulk of the distribution, even if the amplitude of the driving potential was small.
- (c) We have developed a simple 1D kinetic theory, based on the driven Vlasov-Poisson system that describes these chirped-bucket BGK modes. The theory is based on a perturbation scheme, where the driving and the excited wave amplitudes are viewed as perturbations, but uses a heuristic, nonperturbative, space averaged distribution [Eq. (8)] with a localized parabolic depression at the exact resonance as found in simulations. The theory also employs a two-time-scale representation of dependent variables and assumes continuous phase-locking between the driving and driven fields.
- (d) For sufficiently hot and dense plasmas, our theory predicts excitation of large amplitude, undamped, multi-peaked driven-bucket BGK modes {type-I solutions [Eq. (31)]} for a down-chirped driving frequency. Existence of these synchronized waves, their persistence after the driving field is switched off, and many fea-

tures predicted by the theory have been confirmed in recent experiments<sup>13</sup> and self-consistent simulations.

- (e) Similar to spontaneously generated BGK modes,<sup>9–12</sup> *adiabaticity* is a necessary ingredient of the suggested excitation method. However, in our case, the adiabaticity can be controlled by the chirp rate of the driving frequency, rather than through internal processes. This external control yields a convenient way of creating slowly adjusting, nearly perfect equilibrium BGK structures.
- (f) Both the driving and excited fields in our theory were treated as perturbations. Thus, we have left the study of some important phenomena associated with larger amplitude chirped-bucket BGK modes for future work. For example, further research is needed on large, driven multimode excitations and resonance overlap; nonlinear interactions between chirped BGK modes with different mode numbers; loss of adiabaticity and dephasing due to a faster growth of the excited wave; and 3D effects. Finally, studying the excitation of similar BGK modes in other, externally driven plasma configurations seems promising.
- (g) We have also performed self-consistent numerical simulations of excitation of synchronized BGK modes. Our 1D PIC code allowed us to confirm the main results of the small amplitude theory and yielded good qualitative agreement with experiments for large amplitude excitations. We plan to further use this code in analyzing many of the above-mentioned nonlinear effects.

## ACKNOWLEDGMENTS

This work was supported by the NSF, Division of High-Energy Physics, USDOE, and Israel Science Foundation Grant No.187/02. One of the authors (L.F.) would like to thank the UNC Berkeley plasma physics group for providing an excellent environment for this research and for hospitality during a sabbatical leave from the Hebrew University.

<sup>1</sup>A. Trivelpiece and R. Gould, J. Appl. Phys. **30**, 1784 (1959).

<sup>2</sup>I. B. Bernstein, J. M. Greene, and M. D. Kruskal, Phys. Rev. **108**, 546 (1957).

<sup>3</sup>H. Schamel, Phys. Plasmas **7**, 4831 (2000).

<sup>4</sup>C. B. Warton, J. Malmberg, and T. O'Neil, Phys. Fluids **11**, 1761 (1968).

<sup>5</sup>J. D. Moody and C. F. Driscoll, Phys. Plasmas **2**, 4482 (1995).

<sup>6</sup>G. Hart and B. G. Peterson, in *Non-Neutral Plasma Physics IV: Workshop on non-Neutral Plasma*, edited by F. Anderegg, C. F. Driscoll, and L. Schweikhard (AIP, New York, 2002), p. 341.

<sup>7</sup>R. E. Ergun, C. W. Carlson, J. P. McFadden, *et al.*, Phys. Rev. Lett. **81**, 826 (1998).

<sup>8</sup>J. Danielson, Ph.D. thesis, University of California-San Diego, 2002.

<sup>9</sup>H. L. Berk, B. N. Breizman, and M. S. Pekker, Plasma Phys. Rep. **23**, 778 (1997).

<sup>10</sup>B. N. Breizman, H. L. Berk, and M. S. Pekker, Phys. Plasmas **4**, 1559 (1997).

<sup>11</sup>H. L. Berk, B. N. Breizman, J. Candy, M. Pekekr, and N. V. Petviashvili, Phys. Plasmas **6**, 3102 (1999).

<sup>12</sup>D. Yu. Eremin and H. L. Berk, Phys. Plasmas **9**, 772 (2002).

<sup>13</sup>W. Bertsche, J. Fajans, and L. Friedland, Phys. Rev. Lett. **91**, 265003 (2003).

<sup>14</sup>R. C. Davidson, *Physics of Nonneutral Plasmas* (Addison-Wesley, Redwood City, 1990), p. 42.

<sup>15</sup>G. M. Zaslavskii and B. V. Chirikov, Usp. Fiz. Nauk **105**, 3 (1971) [Sov. Phys. Usp. **14**, 549 (1972)].

<sup>16</sup>T. H. Stix, *Waves in Plasmas* (AIP, New York, 1992), p. 206.

<sup>17</sup>C. K. Birdsall and A. B. Langdon, *Plasma Physics via Computer Simulation* (McGraw-Hill, New York, 1985).